

CHANDRA X-RAY IMAGING SPECTROSCOPY OF THE YOUNG SUPERNOVA REMNANT KESTEVEN 75

DAVID J. HELFAND, BENJAMIN F. COLLINS, AND E. V. GOTTHELF

Columbia Astrophysics Laboratory, Columbia University, 550 West 120th Street, New York, NY 10027, USA;
djh@astro.columbia.edu; bfc@astro.columbia.edu; evg@astro.columbia.edu

Version of Sep 17 2002

ABSTRACT

We present a spatially resolved spectroscopic analysis of the young Galactic supernova remnant Kes 75 (SNR G29.7-0.3) using the *Chandra* X-ray Observatory. Kes 75 is one of an increasing number of examples of a shell-type remnant with a central pulsar powering an extended radio/X-ray core. We are able to pinpoint the location of the recently discovered pulsar, PSR J1846–0258, and confirm that X-rays from the remnant’s core component are consistent with non-thermal power-law emission from both the pulsar and its surrounding wind nebula. We find that the spectrum of the pulsar is significantly harder than that of the wind nebula. Fainter, diffuse emission is detected from throughout the volume delineated by the radio shell with a surface brightness distribution strikingly similar to the radio emission. The presence of strong lines attributable to ionized Mg, Si, and S indicate that at least some of this emission is thermal in nature. However, when we characterize the emission using a model of an underionized plasma with non-solar elemental abundances, we find we require an additional diffuse high-energy component. We show that a significant fraction of this emission is an X-ray scattering halo from the pulsar and its wind nebula, although a nonthermal contribution from electrons accelerated in the shock cannot be excluded.

Subject headings: pulsars: individual (PSR J1846–0258); supernova remnants: individual(G29.7-0.3); star: individual (PSR J1846–0258); stars: neutron; X-rays: general

1. INTRODUCTION

The expected products of a core-collapse supernova include a shock wave propagating into the circumstellar/interstellar medium, metal-enriched ejecta from the progenitor star moving outward behind the shock, and a collapsed remnant of the stellar core (often a rapidly spinning, magnetized neutron star). These products should manifest themselves as a limb-brightened shell of radio emission at the outward-moving shock, an interior volume of hot, shocked gas and stellar ejecta emitting thermal X-rays, a short-period radio and/or X-ray-/ γ -ray pulsar, and a bright central nebula driven by the pulsar’s relativistic outflow. To date, more than 1300 pulsars (Manchester et al. 2002), 230 radio supernova remnant (SNRs – Green 2001) (80 with thermal X-ray emission), and two dozen pulsar wind nebulae (PWNe – Kaspi and Helfand 2002) are known in the Milky Way; the only problem is that they are seldom all found in the same place. The rare coincidences that actually match our expectations for the grave sites of massive stars are called composite supernova remnants (Weiler 1983; Helfand and Becker 1987).

The Galactic radio source Kes 75 (SNR G29.7-0.3) is a prototypical example of a composite remnant. It exhibits a limb-brightened, 3/5-diameter radio shell with a steep spectrum ($\alpha \sim -0.7$, where $S(\nu) = S(\nu_0)\nu^\alpha$) and modest radio polarization, surrounding a flat-spectrum ($\alpha \sim 0.0$), highly polarized radio core first detected in X-rays by the Einstein Observatory (Becker, Helfand & Szymkowiak 1983). Neutral hydrogen absorption measurements show the source to lie beyond the solar circle on the far side of the Galaxy at a distance of ~ 19 kpc (Becker & Helfand 1984). Observations by the Advanced Satellite for Cosmology and Astrophysics (*ASCA*) verified the existence

of both thermal and nonthermal emission, but lacked the spatial resolution necessary to separate the components (Blanton & Helfand 1996). A recent observation with the X-ray Timing Explorer led to the discovery of a young, energetic X-ray pulsar, PSR J1846–0258, with a characteristic age of 723 yrs. The pulsar was localized to within 1’ of the remnant core using an *ASCA* observation (Gotthelf et al. 2000). Recent pulsar timing observations suggest that the true age of the remnant could be between 980 and 1770 years (Mereghetti et al. 2002).

We report here the results of an observation of Kes 75 with the *Chandra* X-ray Observatory. We utilize the spatial resolution of *Chandra* to determine an accurate location for PSR J1846–0258, finding it at the center of a highly structured pulsar wind nebula. The spectral properties of the pulsar, its nebula, and the surrounding shell are explored, yielding evidence for a nonthermal component coincident with the thermal shell X-ray emission. In §2 we describe the observations and data reduction procedures. In §3 we detail our imaging results, while in §4 and §5 we present our spectral results on the core and shell components, respectively. We conclude (§6) with a discussion of these results and their implications for Kes 75 itself, and for the class of composite remnants in general.

2. OBSERVATIONS

Our observation of Kes 75 was obtained on 10 – 11 Oct 2000 with the *Chandra* X-ray Observatory (Weisskopf, O’Dell, & van Speybroeck 1996). Photons were collected using the Advanced CCD Imaging Spectrometer (ACIS), a mosaic of ten X-ray CCD chips, with the target placed on the ACIS–S3 chip, offset 2’ from the nominal aimpoint to avoid losing portions of the remnant to the CCD gaps. The back-side illuminated ACIS–S3 CCD is sensi-

tive to photons in the $\sim 0.2 - 10$ keV energy range with a spectral resolution of $E/\Delta E \sim 10$ at 1 keV. The on-axis angular point-spread function (PSF) of the telescope is $\sim 0''.5$ at 1 keV and is undersampled by the CCD pixels ($\sim 0''.49 \times 0''.49$). As a consequence of the 3 s CCD readout time, no timing information for the pulsar ($P = 324$ ms) is available with the ACIS instrument.

Data reduction and analysis were performed using the CIAO, FTOOLS, and XSPEC X-ray analysis software packages. To correct for the detrimental effects of charge transfer inefficiency (CTI) on the gain and resolution of the CCD, we reprocessed the Level 1 event data using the custom software of Townsley et al. (2000). The resulting CTI-corrected Level 2 event file was then time-filtered to exclude intervals of unacceptably high background activity caused by flares in the rate of solar cosmic ray particles. These intervals were identified using a 3σ iterative clipping algorithm applied to a lightcurve created using all data on the ACIS-S3 chip but with the supernova remnant emission excluded (defined as emission from a radius of $r > 100''$ centered on the SNR radio shell). The subsequent time-filtering resulted in a useful exposure of 33.7 ks. The instrument response files used in the spectral fits were calculated using the RMF and quantum efficiency uniformity (QEU) calibration files that accompany the CTI-removing software.

3. IMAGE ANALYSIS

Figure 1 shows the *Chandra* X-ray view of the supernova remnant Kes 75. As expected, we resolve a bright point-like source at the center of the SNR shell, embedded in a compact X-ray nebula. We take this as a detection of PSR J1846–0258 whose flux of 0.12 ct s^{-1} accounts for $\sim 15\%$ of the 1–7 keV emission from the core component (pulsar + compact nebula) of the remnant. Superposed on the X-ray image are 20 cm radio contours derived from data being taken for our new VLA Galactic Plane survey (Helfand et al. 2001). The similarity between the two images is striking: the core synchrotron nebula, the diffuse shell emission, and the two limb-brightened areas in the southeast and southwest quadrants of the shell are all co-spatial.

The astrometry given in our *Chandra* event file contains known systematic errors¹. To derive an accurate position for PSR J1846–0258, we first corrected the astrometry following the prescription recommended by the CXC². We then ran the source-finding CIAO tool CELLDETECT with a signal-to-noise threshold of 2.5 (employing LDETECT background determinations) in order to locate sources with possible stellar counterparts which could be used to determine the accuracy of the corrected coordinates. Comparing the resulting source positions to the USNO astrometric catalog (Monet 1996) we found five coincidences. One of these lies on top of the bright southwestern filament which affected the X-ray source position determination; this was excluded from further consideration. We then refined the *Chandra* positions by spatially fitting each source with a model PSF using SHERPA. We included a constant background level in this model to al-

low for the bright nebular emission. The weighted root-mean-squared average of the offsets between our calculations and the coincident USNO star positions is $0''.3$, of the same order as the typical uncertainty of the USNO catalog (Deutsch 1999) and of the expected *Chandra* astrometric uncertainty. The computed offsets of $\Delta\text{R.A.} = -0''.04$ and $\Delta\text{Dec} = 0''.09$ confirms the accuracy of the corrected *Chandra* astrometry. The spatial fit for the position of the pulsar yields J2000 coordinates $18^{\text{h}}46^{\text{m}}24.94^{\text{s}} \pm 0.01$, $-02^{\circ}58'30''.1 \pm 0.2$. Comparison with the model PSF confirms the detection of PSR J1846–0258 as an unresolved point-source.

4. SPECTRAL ANALYSIS

It is clear from the image shown in Figure 1 that PSR J1846–0258 is embedded within a pulsar wind nebula. A complete spectral analysis of the pulsar requires a model of the wind nebula to use as a background component. It is further found to be necessary to account for the effects of pile-up on the pulsar spectrum (to be discussed in §4.2). In the following, we first determined the absorbing column density from spectral fits to the PWN whose spectrum is not distorted by pile-up. In the subsequent fits to the pulsar spectrum we fix the absorbing column to this value and use the PWN model as an additive spectral component. Background subtraction for the pulsar wind nebula itself was accomplished using a region southwest of the nebula but within the SNR shell in order to account for any shell emission underlying the nebula; for the remainder of the remnant, background estimates were obtained from a source-free area on the ACIS-S3 chip approximately $4'$ northwest of the remnant; errors in the count rates for all regions resulting from background uncertainties are $\leq 2\%$.

For all spectral fitting presented herein the analysis is restricted to the energy range of 1–7 keV. Below 1 keV, few source photons are detected owing to the high absorption column density to the remnant; above 7 keV the spectrum falls off for all models. Spectra were grouped to contain a minimum of 20 counts bin^{-1} and all errors on the spectral fits are quoted for a $1-\sigma$ confidence range. For spectra extracted from extended regions, it is no longer sufficient to use an instrumental response appropriate for a point source imaged at a single location on the detector. We have therefore employed a user-supplied algorithm created by A. Vikhlinin³ for these regions to produce a count-weighted response function in $16'' \times 16''$ bins, averaged over each extraction aperture.

4.1. The Pulsar Wind Nebula

Surrounding the pulsar is a highly structured diffuse nebula, $\sim 26''$ by $\sim 20''$ in extent, similar to that seen in several other high-resolution *Chandra* images of pulsar wind nebulae (Gotthelf 2001 and references therein). The morphology is generally axisymmetric about a line $\sim 30^\circ$ east of north, with hot spots along this axis on either side of the pulsar. A blow-up of the core region of Kes 75 is shown in Figure 2.

To derive the flux from the pulsar wind nebula, we define an elliptical region with the pulsar region excluded

¹ See <http://cxc.harvard.edu/cal/ASPECT>

² See http://cxc.harvard.edu/cal/ASPECT/fix_offset/fix_offset.cgi

³ available at asc.harvard.edu/cont-soft/software/calcrmf.1.08.html

(as shown in Figure 2a); this region contains a total of $\sim 23,000$ background-subtracted counts. Given the small extent of the nebula and the fact that it lies within a single (FEF) response region, we used the point source response matrix derived for the position of the pulsar. The PWN spectrum is well characterized by an absorbed power-law model which results in a spectral fit with $\chi^2_\nu = 0.97$ for 256 DoF. The best fit model parameters were $\Gamma = 1.92 \pm 0.04$ and $N_H = 3.96 \pm 0.08 \times 10^{22} \text{ cm}^{-2}$. The unabsorbed flux in the 0.5 – 10 keV band from the nebula is $4.0 \times 10^{-11} \text{ ergs cm}^{-2} \text{ s}^{-1}$. The ACIS spectrum and best fit model for the wind nebula region is shown in Figure 3.

To explore the possibility of spectral variations within the nebula, we analyzed several morphologically distinct regions. These included a 2×2 square grid of $17''$ cells centered on PSR J1846–0258, two annular regions from $2''$ – $6''$ and $6''$ – $15''$, and several elliptical regions around distinct features of the wind nebula including the northern and southern lobes and the knot-like feature present in each (see Figure 2b for a definition of the latter regions). The pulsar radiation was excluded in all cases by deleting a $2''$ -radius region around it. All regions are well-fit with a simple power-law plus absorption model, and in each case the spectral parameters derived agree to within 2σ both with each other and with the fit derived for the nebula as a whole (e.g., see Figure 4). In particular, there is no evidence for hardening of the spectrum with increasing distance from the pulsar such as has been seen in G21.5-0.9 (Slane et al. 2000) and 3C58 (Bocchino et al. 2001) and ascribed to synchrotron losses. Table 1 summarizes these results.

4.2. PSR J1846–0258

A spectrum of the pulsar was obtained by extracting counts from within a radius of $2''$ centered on the pulsar’s position. The spectrum contains a total of 4004 counts (including only ~ 10 background counts, but, assuming a nebular surface brightness equal to that in the surrounding $2 - 4''$ annulus, a $\sim 15\%$ contamination from nebular background underlying the source region). A naive fit to a simple power-law model including the effects of interstellar absorption adequately describes the data, yielding a reduced $\chi^2 = 0.9$ for 50 degrees of freedom (DoF). The spectral index of 1.02 ± 0.10 is somewhat flatter than that of the Crab pulsar, but is similar to recently derived indices for other young pulsars including Vela (Pavlov et al. 2001), PSR J2229+6122 (Halpern et al. 2001), and PSR 0540-69 in the LMC (Wang and Gotthelf 2000). However, the estimated pile-up fraction based on the count rate is of order $\sim 10\%$, an effect that tends to flatten the observed spectral index. The inferred column density is $N_H = 3.2 \pm 0.2 \times 10^{22} \text{ cm}^{-2}$ although, again, any artificial flattening of the spectrum resulting from pile-up will likely bias N_H to lower values given the tight correlation between the two parameters (see Figure 4).

Our ultimate model for the pulsar spectrum consists of four components: interstellar absorption, CCD pile-up, a power-law describing the pulsar, and another power-law describing the nebular background. We fixed the column density to $3.96 \times 10^{22} \text{ cm}^{-2}$ and the slope of the background power-law to 1.92, both results of fitting an

absorbed power-law to the wind nebula emission. From our estimate above, we fixed the normalization of the background power-law to 15% of the normalization of the source power-law (varying this fraction from 10% to 20% had no significant effect on the pulsar’s spectral index). Fitting for the slope and normalization of the source power-law as well as the grade-morphing parameter of the pile-up model⁴, we performed a thorough search of the parameter space to find the global minimum. The result is a somewhat steeper spectral index for the pulsar emission of $\Gamma = 1.39 \pm 0.04$. This fit implies a pile up fraction of 8%, consistent with the expected value, and a corrected non-thermal flux from the pulsar of $9.50 \times 10^{-12} \text{ ergs cm}^{-2} \text{ s}^{-1}$ in the 0.5 – 10 keV band. The spectrum of both the pulsar and the wind nebula are displayed in Figure 3, along with residuals from the best fit models detailed in Table 1. Based on the nebula’s power-law index, the pulsar’s spectral index is consistent with that predicted by the empirical relationship of Gotthelf and Olbert (2001) and lies near the mean of these quantities derived for similar young pulsars with wind nebula (see Table 1 of Gotthelf and Olbert 2001).

We also looked for low-energy excess X-ray flux which could represent surface thermal emission from the young neutron star (see the residuals for the four lowest energy spectral points in Figure 5). Although the number of counts present does not allow for a detailed analysis, we fitted for a power-law index restricted to the 2 – 7 keV range where any thermal surface emission is expected to be negligible. This yields $\Gamma = 1.31 \pm 0.06$ (Figure 5). Holding this value (and the nebular N_H) fixed provides an estimate for the blackbody temperature of $kT = 0.16 \pm 0.03 \text{ keV}$, close to the expected temperature of $1.8 \times 10^6 \text{ K}$ for standard cooling of a $\sim 1,000$ -year-old neutron star (e.g., Umeda et al. 1994). However, the error on the normalization is sufficiently large that no meaningful measure of the emitting area is possible.

5. EMISSION FROM THE SUPERNOVA REMNANT SHELL

In order to examine the spectral properties of the shell emission, we have again defined several areas of interest (see Figure 6). We considered i) the entire shell, defined as a circular aperture with a radius of $100''$ centered on PSR J1846–0258 and excluding the elliptical region containing the pulsar and its nebula, ii) an ellipse around each of the ‘clumps’ in the south, and iii) three annuli defined so as to correspond roughly with the boundaries of these (now excluded) ellipses.

As a starting point from which to analyze the thermal shell, we extracted a spectrum of everything outside the pulsar wind nebula to a radius of $\sim 100''$. We fitted a model consisting of interstellar absorption, a thermal bremsstrahlung continuum, and three Gaussians representing the strongest emission lines, in order to compare our results with a similar fit applied to the *ASCA* data by Blanton & Helfand (1996). The positions of the three Gaussians are all consistent with the *ASCA* analysis, and correspond to the ions Mg XI, Si XIII, and S XV. The best-fit emission temperature, $kT = 2.99 \pm 0.12 \text{ keV}$, is significantly discrepant with the *ASCA* and BeppoSAX (Mereghetti et al. 2002) values, however, a consequence of

⁴ See <http://space.mit.edu/%7Edavis/papers/pileup2001.ps>

the inability of the latter observations to distinguish spatially the various remnant components (see below). The FWHM of the Si line offers a crude estimate of the remnant expansion velocity of $\sim 3700 \text{ km s}^{-1}$.

The heuristic model is also useful in searching for spatial variations in the shell spectrum. We constructed fits for the two bright features separately, for the diffuse emission outside these regions, and for three annuli, as well as for the entire remnant (in all cases excluding the synchrotron core). The results are displayed in Table 2. In all cases, the derived N_H is significantly below that derived from the power-law fit to the pulsar wind nebula; in some cases it is, unphysically, less than the measured neutral hydrogen column density (§5), indicating an excess in soft flux over that accounted for by the bremsstrahlung continuum. The derived temperatures suggest a gradient, decreasing from the inside out, also suggestive of a problem with the model. The line centroids are largely constant throughout. Unconstrained models of a Raymond-Smith thermal plasma (Raymond & Smith 1977), as well as multi-temperature plane-parallel shock, and non-equilibrium ionization models (Hamilton *et al.* 1983; Borkowski *et al.* 1994; Liedahl *et al.* 1995; Borkowski *et al.* 2000), including interstellar absorption and varying abundances, all do a poor job of fitting the spectrum.

The problem common to all of the thermal fits is that, in order to account for the observed spectrum at higher energies, the continuum temperature is forced to relatively high values inconsistent with the line strengths, line centroids, and continuum shape below 2 keV (Figure 7). For the *ASCA* and *BeppoSAX* data in which the synchrotron nebula was not resolved from the shell emission, this extra hard flux was simply absorbed into the power-law component. By isolating and excluding the central nebula's emission, the problem with the shell spectrum becomes apparent.

In order to minimize the number of free parameters, we fixed the column density to the well-determined value from the wind nebula fit: $N_H = 3.96 \times 10^{22} \text{ cm}^{-2}$. We then fitted a non-equilibrium ionization model plus a power-law to account for the high energy flux (Figure 8). The abundances for H, He, C, N, O, Fe, and Ni for which we have no usefully constraining data were held fixed at the solar value, while the ions of Mg, Si, S, and Ca were allowed to vary independently. This produces an acceptable fit ($\chi^2 = 2.15$ for 116 DoF) for the diffuse shell emission excluding the two bright regions in the south. The derived temperature is $\sim 0.7 \text{ keV}$, the power-law index is ~ 1.7 , and the ion abundances are ~ 0.5 solar. The fit to the two clump regions combined (their spectra are statistically indistinguishable) is somewhat worse; the derived temperature is very similar, the abundances are slightly higher, and the power-law index is somewhat flatter (see Table 4). The χ^2 values are artificially high as a consequence of a known problem with the response matrix near 2 keV; the rest of the spectrum matches the model well. Interestingly, the ionization parameter $\tau = n_e t$ is 2.7 times higher for the bright clumps; taking the mean time since the emitting gas was shocked as constant over the face of the remnant,

this implies that the clump density $n_e = 2.7$ times the inter-clump density. The emissivity of the plasma should scale as n_e^2 . In fact, the mean surface brightness of the clumps is just $n_e^2 \sim 8$ times the mean surface brightness of the remaining diffuse emission, lending some credence to the model fits. The total luminosity of the thermal component in the 0.5-10 keV band is nominally $1.8 \times 10^{37} \text{ erg s}^{-1}$; however, given the uncertain temperature and large column density, this estimate could be high by a factor of several. Nonetheless, it one of the most luminous shell remnants in the Galaxy. Possible origins for the diffuse power-law component are discussed below.

6. DISCUSSION

6.1. The distance to Kes 75

Becker and Helfand (1984) presented a 21 cm hydrogen absorption spectrum for Kes 75 which shows clear evidence of absorption at negative velocities, indicating a location beyond the solar circle; we adopt their distance of 19 kpc. Assuming a hydrogen spin temperature of 100 K, these measurements indicate a neutral atomic hydrogen column density to the source of $\sim 2 \times 10^{22} \text{ cm}^{-2}$. Since roughly half the hydrogen along any line of sight through the Galaxy is either in ionized or molecular form, we should expect an X-ray absorption column density of $\sim 4 \times 10^{22} \text{ cm}^{-2}$, in excellent agreement with that derived from our fit to the pulsar wind nebula spectrum ($3.96 \times 10^{22} \text{ cm}^{-2}$). The lower N_H values found in the various thermal fits reported in Table 2 and 3 are implausible; the discrepancy is probably due to inadequate plasma models. We thus use the wind nebula value in assessing the intrinsic luminosities of all components of the remnant.

6.2. The X-ray luminosity of the pulsar and its PWN

The nonthermal luminosity from the pulsar is $4.1 \times 10^{35} \text{ erg s}^{-1}$ in the 0.5 – 10 keV band, and the luminosity of its wind nebula⁵ is $1.7 \times 10^{36} \text{ erg s}^{-1}$. Both values are second only to the Crab Nebula and its pulsar among known Galactic objects. However, the efficiencies with which this pulsar converts its rotational kinetic energy to X-rays in its magnetosphere and in its surrounding nebula are both greater than the Crab. The pulsar value of $L_{x\text{-pulsar}}/\dot{E} \sim 1.6\%$ is more than six times this value for the Crab, although it is very similar to the value for PSR J0540-693, the 50 ms pulsar in the Large Magellanic Cloud. The value of $L_{x\text{-nebula}}/\dot{E} \sim 6.5\%$ is the highest known – in this case, comparable to that for the Crab, but several times higher than that for PSR J0540-693.

The similarity of the pulsars and their wind nebulae in Kes 75 and PSR 0540-693 is noteworthy. Morphologically, they are two of the best representatives of the composite remnant class, with prominent radio and X-ray shells and bright pulsar-driven synchrotron cores. Their relatively high values of $L_{x\text{-nebula}}/\dot{E}$ could result from the confinement of the outflowing pulsar wind by the evident shells. The characteristic age of PSR 0540-693 is roughly twice that of PSR J1846–0258 (1400 vs 700 yrs), although the detailed optical study of Kirshner *et al.* (1989) found an

⁵ We note here that there is an error in the X-ray luminosities for this source quoted in Blanton and Helfand (1996). The observed, rather than intrinsic, X-ray fluxes were used. The correct values from the *ASCA* analysis ($L_x(0.5 - 8.0 \text{ keV})_{\text{core}} = 2.5 \times 10^{36} \text{ erg s}^{-1}$ and $L_x(0.5 - 8.0 \text{ keV})_{\text{shell}} = 1.1 \times 10^{37} \text{ erg s}^{-1}$) agree well with the values derived here.

expansion velocity for the shell surrounding PSR J0540-693 of $\sim 3000 \text{ km s}^{-1}$ and a dynamical age of $\sim 760 \text{ yrs}$. There are several striking differences between these two systems however: their spin periods, period derivatives (and, thus, inferred magnetic field strengths), and their shell diameters. It is not implausible that very different pulsar birth parameters have led to the difference in the remnant sizes.

6.3. The large shell diameter of Kes 75

The radius of Kes 75, 9.7 pc, is enormous for the young characteristic age of its pulsar, implying a *mean* expansion velocity for the remnant of over $13,000 \text{ km s}^{-1}$. For even a modest $5M_{\odot}$ of material ejected into a vacuum, the kinetic energy required is nearly 10^{52} erg . For $10 M_{\odot}$ of ejecta going off into a medium with a mean density of 0.5 cm^{-3} , the required kinetic energy reaches nearly 10^{53} erg , comparable to the entire gravitational binding energy of the neutron star whose formation produced the explosion. The shell X-ray luminosity derived in §5 suggests a density closer to 1 cm^{-3} . Such kinetic energy values are both unprecedented and highly implausible.

There are several possible ways to reduce the required explosion energy. A smaller distance for the remnant would reduce the inferred velocity, albeit only as $d^{0.5}$. The HI absorption spectrum of Becker and Helfand (1984) leaves little possibility of reducing the distance by more than $\sim 30\%$, in that all velocities are seen in absorption to the solar circle and beyond. Alternatively, the remnant could be considerably older than the pulsar's characteristic age $\tau_c = P/2\dot{P}$. This would run counter to the situation for other remnants. For the Crab, $\tau_c = 1240 \text{ yrs}$, while its true age $t = 945 \text{ yrs}$, for PSR 0540-693 $\tau_c = 1672 \text{ yrs}$ (Zhang et al. 2001) while the dynamical age estimate is 760 yrs , and for PSR J1811.5-1926 in G11.2-0.3, $\tau_c = 24,000 \text{ yrs}$, while its association with SN 386AD means $t = 1616 \text{ yrs}$ (Kaspi et al. 2001); a plausible explanation in each of these cases is that the pulsar's initial period was not negligible compared to its present spin rate (an assumption of the approximation for τ_c defined as above).

Indeed, for a pulsar braking index $n = -\nu\ddot{\nu}/\dot{\nu}^2 = 3$, expected for braking by pure magnetic dipole radiation, the characteristic age is *always* an upper limit to the true age. It is possible for the true age to exceed τ_c , however, if $n < 3$. But for the range of most measured indices ($\sim 1.4 < n < 2.9$), $t \leq 5\tau_c$, and is equal only for a very high initial spin rate, P_0 . The recent results of Mereghetti et al. (2002) suggest a value for n in the range $1.86 < n < 2.48$ depending on the glitch history of the star. For high initial spin rates, this yields ages in the range $980 < t < 1770 \text{ years}$. If we push all the numbers in one direction – reduce the distance to 15 kpc , posit only $5 M_{\odot}$ of ejecta, require an ambient density of $n = 0.1 \text{ cm}^{-3}$, and double the age, thus requiring a small P_0 – the energy needed *just* to explain the observed kinetic energy is $2 \times 10^{51} \text{ ergs}$, at the upper end of the inferred distribution of supernova explosion energies.

A consequence of requiring a fast initial spin rate for PSR J1846–0258 is that, given its enormous magnetic field of $5 \times 10^{13} \text{ G}$, the amount of rotational kinetic energy dumped into the remnant shortly after the explo-

sion will exceed the fraction of the explosion energy itself that couples to the surrounding matter (typically $\sim 1\%$). For $P_0 = 0.01P \sim 3 \text{ ms}$, $E_{rot} = 2.2 \times 10^{51} \text{ ergs}$. As Blanton and Helfand (1996) showed, the current total energy in radio-emitting relativistic particles and magnetic field in the synchrotron nebula is only $\sim 10^{48} \text{ ergs}$. If PSR J1846–0258 had been born with a spin period only a factor of two or so below its current value, it could have just supplied this inferred energy with none left over to help power the expansion of the remnant. However, if it were born spinning a hundred times faster, the current synchrotron nebula represents only $\sim 10^{-4}$ of its total energy output, with the remainder transferred to the kinetic energy of the shell.

6.4. The hard component to the shell emission

As we showed in §4, the X-ray emission from outside the clearly demarcated pulsar wind nebula includes a hard spectral component that is inconsistent with an extension of the thermal emission that accounts for the bulk of the shell's X-ray luminosity. Both a very high-temperature plasma ($T \sim 20 \text{ keV}$) and a power-law can satisfactorily fit the high-energy spectrum. We explore here the possible origins for this emission.

There are two possible sources of relativistic electrons which could contribute to the power-law emission: leakage of pulsar wind nebula particles into the shell cavity, and particles accelerated at the blastwave shock. The first explanation can be shown to be implausible.

There is no strong gradient in the amount of high energy emission with radius; in particular, 5 keV photons in excess of those expected from the low-temperature thermal plasma are found to the edge of the remnant shell. The particle energy required for 5 keV radiation $E \sim 2.7 \times 10^4 \text{ GeV}$. The synchrotron lifetime of such a particle must, at minimum, exceed the light travel time from the pulsar to the rim of the remnant: $\tau_{synch} > c/r \approx 10^9 \text{ s}$ or 32 years . This sets a constraint on the strength of the magnetic field in the remnant $B < 422 \text{ s } \tau_{synch}^{-1} E_{GeV}^{-1} \approx 4 \mu\text{G}$ – comparable to the interstellar field. By contrast, the equipartition field in the pulsar wind nebula is $300 \mu\text{G}$; furthermore, propagation of the particles from the wind nebula boundary to the remnant's rim at c is highly unrealistic, lowering further the allowed field strength within the shell. Thus, it seems highly unlikely that the bulk of the high energy diffuse emission in the remnant is from pulsar-injected particles.

In recent years, synchrotron X-rays from particles accelerated at the outward moving supernova shock have been discovered in several remnants (Allen, Gotthelf & Petre 2000 and references therein; Slane et al. 1999; Slane et al. 2001). The observed power law spectral indices are quite steep, ranging from $\Gamma = 2.4$ in G347.3-0.5 (Slane et al. 1999) to $\Gamma = 3.3$ in RCW 86 (although it should be noted that the XTE results of Allen et al. (2000) on young remnants uses a harder energy band – and yields steeper slopes – than are obtained for the two ASCA synchrotron shells which are fitted in a softer band). Contributions from nonthermal emission to the total X-ray flux in the $1 - 10 \text{ keV}$ band range from a few percent to $> 90\%$.

The fitted power law component in the shell of Kes 75 has a photon index on the flat end of this distribution (al-

though it is not very well-constrained – see Table 4) and an implied luminosity of $\sim 3.2 \times 10^{35}$ erg s $^{-1}$. Given the high shell expansion velocity, it is not implausible that some of this emission is indeed direct synchrotron radiation from high energy electrons. However, when the effect of dust scattering from the PWN is included (see below), the inferred spectral index is flatter than that seen in any other remnant.

One component that must be present at some level arises from the dust-scattering halo of the central nebula plus pulsar (e.g., Mauche and Gorenstein 1986). A substantial literature exists on this topic, although it has been problematic to derive quantitative constraints on the relevant parameters – grain size distribution, composition, internal structure, and distribution along the line of sight – from data of limited spatial resolution. The recent *Chandra* observation of the Galactic X-ray binary GX 13+1 by Smith, Edgar, and Shafer (2002) shows simultaneously the lack of agreement with previous models as well as the sensitivity of such observations to various instrumental effects. Nonetheless, as it provides a direct empirical measurement of dust-scattering effects at the highest available resolution, we use these results to estimate the contamination of the Kes 75 shell by the dust scattering halo of the PWN.

Smith et al. provide radial profiles at three energies for the halo of GX 13+1. We have measured the mean surface brightness in each 10'' annulus from 50'' to 100'' (the outer limit of the remnant shell) and calculated the fraction of scattered flux detected. We have then extrapolated the observed surface brightness to 25'' (the inner boundary of the diffuse shell emission in question) and obtained a crude estimate of the fraction of the intensity scattered into the SNR shell region from the pulsar plus its surrounding nebula (ignoring the effect of the nebula's extent). We obtain values of $\sim 15\%$, $\sim 10\%$, and $\sim 8\%$ for the $\Delta E = 100$ eV energy bands centered at 2.15, 2.95, and 3.75 keV, respectively. As noted by Smith et al., the energy dependence $\sim E^{-1}$ is shallower than the theoretically expected value of E^{-2} . We then correct for the difference in column density between GX 13+1 and Kes 75 ($\sim 2.8 \times 10^{22}$ cm $^{-2}$ vs. $\sim 4 \times 10^{22}$ cm $^{-2}$) by finding τ_{scat} from Figure 4 in Predehl (1997) and using the simple relation for the fractional scattered intensity $I_{frac} = (1 - e^{-\tau_{scat}})$; this increases the estimates above by a factor of 1.2.

In the band 2 – 4 keV, then, it is possible to explain most of the putative power-law emission as a simple dust-scattering halo of the PWN. In the 1 – 2 keV band, however, we would expect a contribution from the halo that exceeds the total power law component. Two effects are relevant here. Mathis and Lee (1991) show that multiple scattering is expected to set in for $\tau_{scat} > 1.3$ and broaden

the halo; for our column density, this limit is exceeded at 1.7 keV, although the effect is not large for the 25'' to 100'' region of interest here. Secondly, the thermal component of the fit absorbs a large (and uncertain) fraction of the power in the 1 – 2 keV band where the Mg and Si lines are found. If some of the photons in this band are in fact attributable to dust scattering, it might well raise the equivalent widths of these lines and boost their sub-solar abundances to (the expected) higher values. It could also help explain the disturbing trend toward lower temperatures at larger shell radii noted above.

In the high energy (4 – 7 keV) band, there appears to be some power law contribution beyond the expected halo emission; whether this is evidence of an unusually flat-spectrum synchrotron contribution from the shell, a small thermal contribution from the fast blastwave shock, or further unexpected scattered flux remains unclear.

A quantitative analysis of the spectrum including all of the effects discussed above is beyond the scope (not to mention the calibration uncertainties and photon counting statistics) of this paper. Less distant remnant shells are better targets for attempts to untangle the complicated physics of thermal and non-thermal X-ray emission. However, the apparent importance of considering dust-scattering in this case should serve as a cautionary tale for observers using the new high-energy imaging capabilities to explore absorbed remnants in the Galactic plane.

6.5. Conclusions

Our high-resolution imaging observations of Kes 75 have revealed all the components expected surrounding the site of recent stellar demise. The young pulsar and its wind nebula are shown to be among the most efficient known at turning rotational kinetic energy into X-ray emission; the extraordinary magnetic field strength of the pulsar may be responsible for this notoriety. Thermal X-ray emission is seen from throughout the remnant shell, although deriving constraints on the remnant's evolutionary state and elemental abundances is compromised by the presence of a significant diffuse nonthermal component which we attribute largely to the dust-scattering halo of the pulsar and its nebula. The presence of such halos needs to be considered when deriving inferences concerning the presence of nonthermal components in the spectra of distant shell-type and composite remnants.

Acknowledgments — D.J.H. acknowledges support from the *Chandra* program through grant SAO G00-1130X, while E.V.G. is supported by NASA LTSA grant NAG5-7935.

REFERENCES

- Allen, G.E., Gotthelf, E.V., and Petre, R. 2000 in "26th International Cosmic Ray Conference" eds. D. Kieda, M. Salamon, & B. Dingus, ICRC proceedings, 3, 480
- Becker, R. H., Helfand, D. J., Szymkowiak, A. E., 1983 ApJ, 268, 93
- Becker, R. H. & Helfand, D. J. 1984, ApJ, 283, 154
- Blanton, E. L. & Helfand, D. J. 1996, ApJ, 470, 961
- Bocchino, F., Warwick, R. S., Marty, P., Lumb, D., Becker, W., & Pigot, C 2001, A&A, 369, 1078
- Borkowski, K. J., Lyerly, W. J. & Reynolds, S. P 2001, ApJ, 548, 820
- Borkowski, K. J., Sarazin, C. L. & Blondin, J. M. 1994, ApJ, 429, 710
- Deutsch, E.W. 1999, AJ, 118, 1882
- Green, D.A. 2001, "A Catalogue of Galactic Supernova Remnants" at <http://www.mrao.cam.ac.uk/surveys/snrs/>
- Gotthelf, E. V., Vasisht, G., Boylan-Kolchin, M. & Torii, K. 2000, ApJ, 542, L37
- Gotthelf, E.V. 2001 in "The 20th Texas Symposium on Relativistic Astrophysics", eds. H. Martel and J. C. Wheeler, AIP conference proceedings

- Gotthelf, E.V. and Olbert, C.M. 2001 in "Neutron Stars in Supernova Remnants" (ASP Conference Proceedings), eds P. O. Slane and B. M. Gaensler (in press); astro-ph/0112017
- Halpern, J.P., Camilo, F., Gotthelf, E.V., Helfand, D.J., Kramer, M., Lyne, A.G., Leighly, K.M., & Eracleous, M. 2001, ApJ, 552, L125
- Hamilton, A. J. S., Sarazin, C. L. & Chevalier, R. A. 1983, ApJS, 51, 115
- Helfand, D. J. & Becker, R.H. 1987, ApJ, 314, 203
- Helfand, D.J., Laird, E.S., Brooks, A.M., Becker, R.H., White, R.L., Warwick, R.S. and Watson, M.G. 2001, BAAS, 33, 1440
- Kapsi, V. and Helfand, D.J. 2002, ASP Conf. Ser. 271: Neutron Stars in Supernova Remnants, 3
- Liedahl, D. A., Osterheld, A. L. & Goldstein, W. H. 1995, ApJ, 438, L115
- Manchester et al. 2002, ASP Conf. Ser. 271: Neutron Stars in Supernova Remnants, 31
- Monet, D. 1996 "USNO A - V1.0" (Washington:US Naval Observatory)
- Mathis, J.S. & Lee, C.-W. 1991, ApJ, 376, 490
- Pavlov, G.G., Zavlin, V.E., Sanwal, D., Burwitz, V., & Garmire, G. 2001, ApJ, 552, L129
- Predehl, P. 1997 Ap&SS, 258, 89
- Raymond, J. C. & Smith, B. W. 1977, ApJS, 35, 419
- Slane, P., Gaensler, B.M., Dame, T.M., Hughes, J.P., Plucinsky, P.P., and Green, A. 1999, ApJ, 525, 357
- Slane, P., Chen, Y., Schulz, N.S., Seward, F.D., Hughes, J.P., & Gaensler, B.M. 2000, ApJ, 528, L109
- Slane, P. Hughes, J.P., Edgar, R.J., Plucinsky, P.P., Miyata, E., Tsunemi, H., and Aschenbach, B. 2001, ApJ, 548, 814
- Smith, R.K., Edgar, R.J., & Shafer, R.A. 2002, astro-ph/0204267
- Townsley, L. K., Broos, P. S., Garmire, G. P. & Nousek, J. A. 2000, ApJ 534, L139
- Umeda, H., Nomoto, K., Tsuruta, S., Muto, T. & Tatsumi, T. 1994, ApJ, 431, 309
- Wang, Q.D. & Gotthelf, E.V. 2000, ApJ, 532,L117
- Weiler, K. W. 1983, IAU Symp. 101: Supernova Remnants and their X-ray Emission, 101, 299
- Weisskopf, M. C., O'Dell, S. L., & van Speybroeck, L. P. 1996, Proc. SPIE, 2805, 2
- Zhang, W., Marshall, F. E., Gotthelf, E. V., Middleditch, J., Wang, Q. D. 2001, ApJ 554, L177

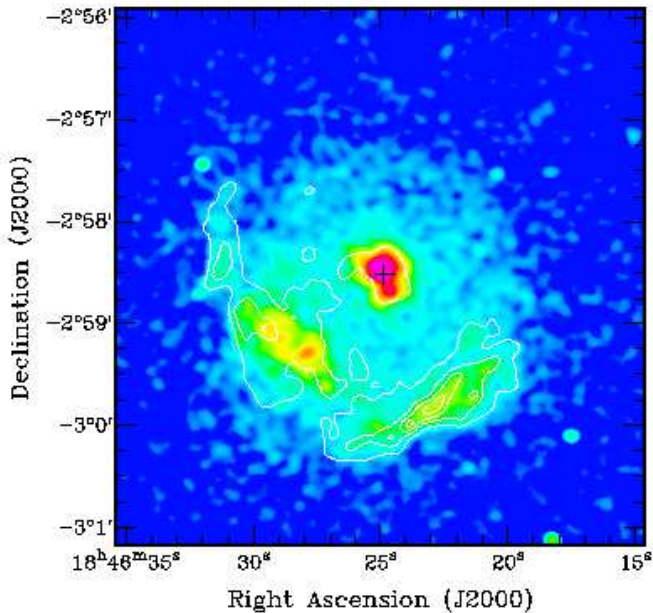


FIG. 1.— The X-ray view of Kes 75 and its central pulsar wind nebula in the 1.0 – 7.0 keV energy band, as obtained with the ACIS instrument on-board the *Chandra* Observatory. The pulsar PSR J1846–0258 resides at the center of wind nebula. The false color image is displayed with a logarithmic intensity scale. Overlaid are the VLA 20 cm radio image contours. The X-ray image has been smoothed with an elliptical Gaussian function to match the radio image which has a synthesized beam of $6''.2 \times 5''.4$. The similarity of the morphology in the two wavelength regimes is apparent. The cross marks the position of the pulsar; the point source is not apparent because the high-surface-brightness pixels have been saturated to show the structure of the lower surface brightness emission.

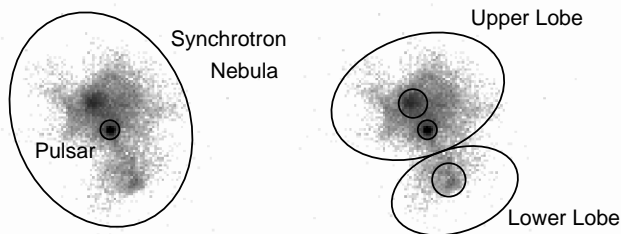


FIG. 2.— A blown-up X-ray view of the center of Kes 75 showing the pulsar wind nebula emission surrounding PSR J1846–0258, as obtained with the ACIS-S3 instrument on-board the *Chandra* Observatory. **(Left)** – The central circle illustrates the aperture used to extract photons from the pulsar, while the ellipse denotes the area (with the circle excluded) used for extracting PWN photons. **(Right)** – Same view as the adjacent panel showing one of the sets of regions used in our morphological analysis of the pulsar wind nebula (see §4.1). The circles flanking the pulsar aperture isolate two bright spots. The region of the pulsar aperture is excluded from the upper-lobe area. The unbinned and unsmoothed image in both panels is displayed with a logarithmic intensity scale.

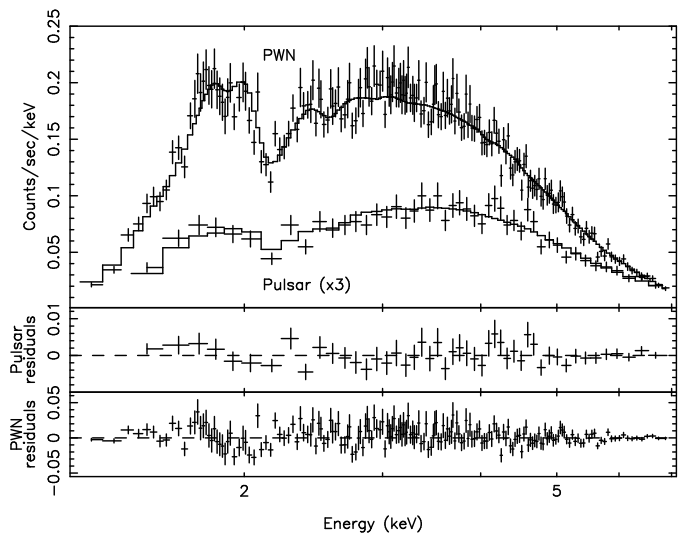


FIG. 3.— Spectra and residuals for an absorbed power-law model fit to the data from PSR J1846–0258 and the surrounding PWN. Spectra were extracted using the regions shown in Figure 2a. Both spectra are grouped to contain a minimum of 20 counts per spectral bin. The pulsar spectrum has been corrected for pile-up and background contamination following the procedure described in §4.2

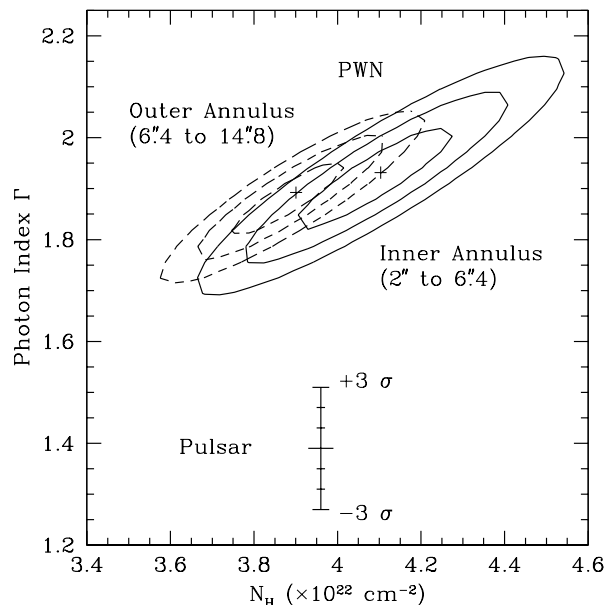


FIG. 4.— Confidence contours for two interesting parameters for model fits to inner and outer regions of the pulsar wind nebula using a simple absorbed power-law model. No evidence for a steepening of the power law index with radius is apparent. The photon index for the pulsar (derived with holding the N_H value fixed at the best-fit nebular value) is significantly flatter than that of the nebula after taking full account of source pileup (see text for details).

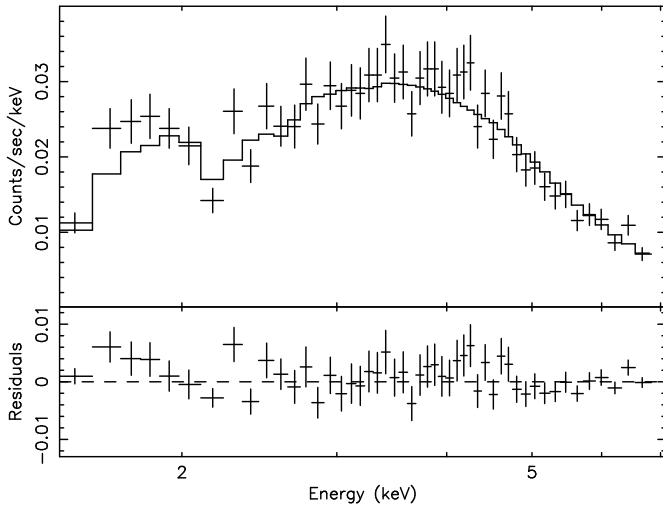


FIG. 5.— Best fit model for the spectrum of PSR J1846–0258 using only the 2–7 keV band to search for a putative blackbody component. Note the apparent excess in the four lowest spectral channels. The model has been corrected for pile-up and background contamination following the procedure described in §4.2

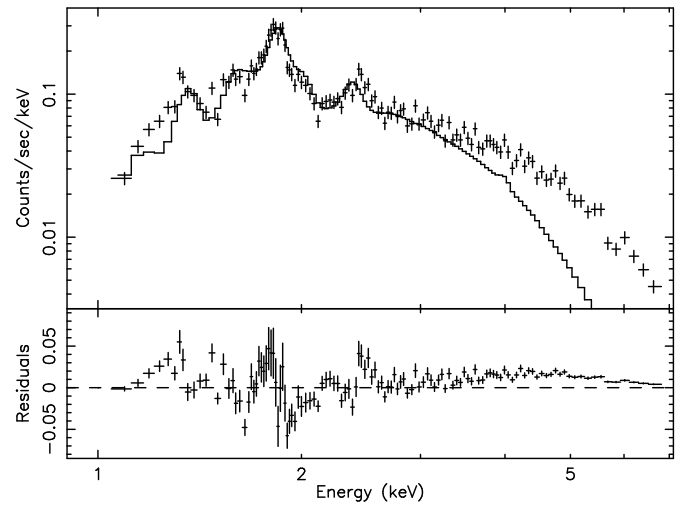


FIG. 7.— Spectrum and model fit to the diffuse emission from Kes 75. Shown is the best fit non-equilibrium ionization collisional plasma model. The failure of this model to fit both the emission lines and the hard continuum simultaneously properly is obvious.

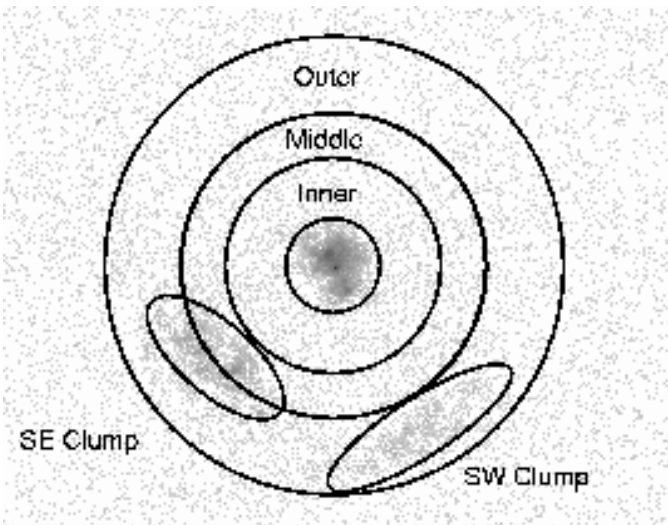


FIG. 6.— Extraction regions used for the spectral analysis of the thermal emission from Kes 75 showing the inner, middle, and outer annuli and the two clumps. The unbinned and unsmoothed image is displayed with logarithmic intensity

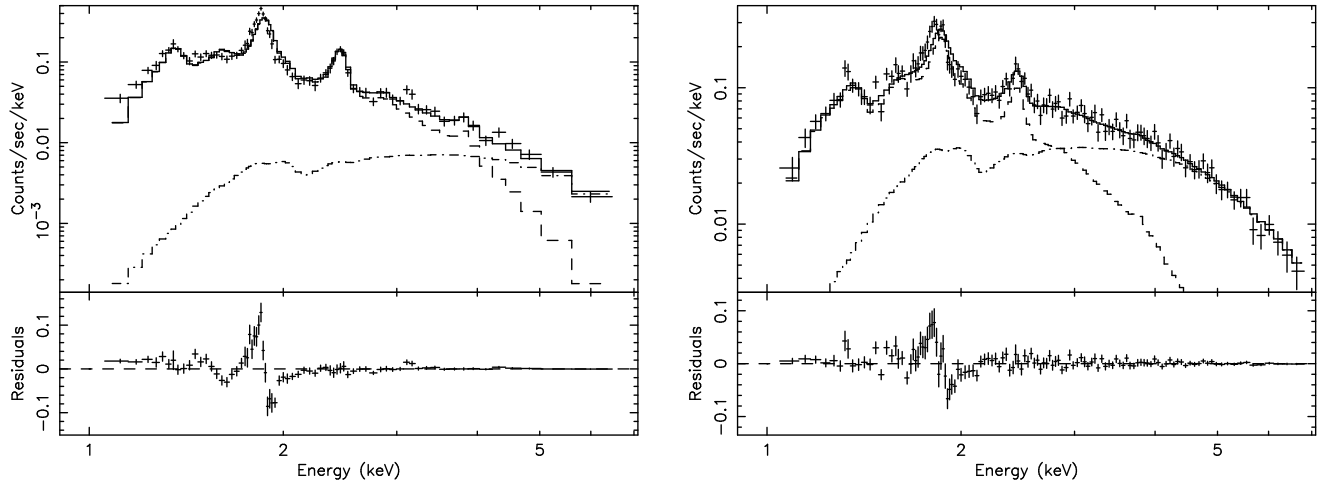


FIG. 8.— Spectra from two regions of the thermal shell of Kes 75. These spectra are fitted with a two component model including both a non-equilibrium ionization collisional plasma model plus a power-law component. **Left** – the spectra and best fit model for the south eastern clump. **Right** – The same model as applied to the diffuse emission region. In both cases the power-law component fits the higher end of the spectrum very well, lowering the temperature of the thermal component to a more reasonable value. The dominate feature around 2 keV in the residual plots are most likely due to a known response matrix calibration issue.

TABLE 1
SPECTRAL FITS TO PSR J1846–0258 AND ITS PWN

Region	N_H ($\times 10^{22}$ cm $^{-2}$)	Photon Index	Flux ^a (ergs cm $^{-2}$ s $^{-1}$)	χ^2_ν (DoF)
Pulsar ^b	3.96 (fixed)	1.39 ± 0.04	0.95×10^{-11}	1.1 (425)
Pulsar Wind Nebula	3.96 ± 0.08	1.92 ± 0.04	4.0×10^{-11}	0.97 (256)
Inner Annulus	4.08 ± 0.13	1.92 ± 0.07	...	1.11 (146)
Outer Annulus	3.88 ± 0.10	1.88 ± 0.05	...	1.04 (259)

^aFlux quoted for the 0.5 – 10 keV energy range.

^bThis model requires additional processing due to the effects of CCD pileup; the procedure used to produce this corrected spectrum is described in the text.

TABLE 2
SPECTRAL FITS TO THE KES 75 THERMAL SHELL (SELECTED REGIONS)

Parameter ^a	SE Clump	SW Clump	Faint Diffuse	entire SNR
N_H (10^{22} cm $^{-2}$)	1.69 ± 0.04	1.74 ± 0.08	1.79 ± 0.07	1.74 ± 0.03
kT	1.79 ± 0.07	2.44 ± 0.22	5.02 ± 0.60	2.99 ± 0.12
Mg XI:				
E	1.325 ± 0.006	1.330 ± 0.008	1.310 ± 0.008	1.321 ± 0.004
σ_E (keV)	0	0	0	0
Si XIII:				
E	1.827 ± 0.002	1.826 ± 0.004	1.814 ± 0.004	1.825 ± 0.002
σ_E	0	0	0.027 ± 0.007	0.010 ± 0.006
S XV:				
E	2.436 ± 0.004	2.430 ± 0.008	2.400 ± 0.018	2.427 ± 0.005
σ_E	0	0.019 ± 0.027	0.146 ± 0.021	0.046 ± 0.008
χ^2_ν (DoF)	1.22 (60)	1.77 (58)	1.21 (113)	1.37 (142)

^aAll units of energy are in keV. Spectral fits in the 1 – 7 keV energy range.

TABLE 3
SPECTRAL FITS TO THE KES 75 THERMAL SHELL (RADIAL REGIONS)

Parameter ^a	Inner	Middle	Outer
N_H	2.45 ± 0.09	2.30 ± 0.11	1.84 ± 0.08
kT	4.87 ± 0.58	4.23 ± 0.63	3.11 ± 0.32
Mg XI:			
E	1.226 ± 0.029	1.301 ± 0.014	1.316 ± 0.007
σ_E	0	0	0
Si XIII:			
E	1.800 ± 0.009	1.797 ± 0.014	1.826 ± 0.005
σ_E	0	0.032 ± 0.022	0.032 ± 0.010
S XV:			
E	2.474 ± 0.033	2.401 ± 0.051	2.409 ± 0.016
σ_E	0.074 ± 0.057	0.129 ± 0.050	0.077 ± 0.024
χ^2_ν (DoF)	1.12 (31)	1.10 (34)	1.17 (59)

^aAll units of energy are in keV. Spectral fits in the 1 – 7 keV energy range.

TABLE 4
SPECTRAL FITS TO THE KES 75 THERMAL SHELL (W/ HARD COMP. MODEL)

Parameter ^a	Diffuse Emission	Clump Emission
N_H ($\times 10^{22}$ cm ⁻²)	3.96 (fixed)	3.96 (fixed)
<i>Abund. Allowed to Varying in Fixed Ratios</i>		
Γ	2.71 ± 0.04	3.02 ± 0.09
kT	0.39 ± 0.01	0.66 ± 0.01
Abund. (Z/Z_\odot)	13.6 ± 0.4	2.2 ± 0.3
τ ($\times 10^{11}$ s cm ⁻³)	$4.31^{+0.91}_{-0.66}$	$2.33^{+0.25}_{-0.23}$
χ^2_ν (DoF)	2.73 (119)	4.60 (135)
<i>Abund. Allowed to Vary Individually^b</i>		
Γ	1.72 ± 0.07	1.34 ± 0.14
kT	0.69 ± 0.01	0.68 ± 0.01
Mg	0.35 ± 0.04	1.03 ± 0.05
Si	0.25 ± 0.02	0.66 ± 0.02
S	0.49 ± 0.06	0.98 ± 0.05
Ca	0.35 ± 0.60	1.90 ± 0.69
τ ($\times 10^{11}$ s cm ⁻³)	0.809 ± 0.060	$2.20^{+0.24}_{-0.21}$
Flux ^c (ergs cm ⁻² s ⁻¹)	2.54×10^{-10}	1.66×10^{-10}
χ^2_ν	2.15 (216)	3.81 (132)

^aAll units of energy are in keV. Spectral fits in the 1–7 keV energy range.

^bOnly the elements whose emission lines are primarily within the energy range of our data have been fit as free parameters; the abundances of the elements with lines outside of that range have been fixed to the solar values.

^cFlux quoted for the 0.5 – 10 keV energy range.